Image calibration in the OmegaCAM pipeline and a proper motion survey for old halo white dwarfs

Ewout Helmich

September 30, 2003

Master's Thesis
supervised by Dr. Edwin A. Valentijn

Introduction

This project divides broadly into two parts. The first comprised of writing the Python code for the part of the OmegaCAM data reduction ("calibration") pipeline that has to do with combining the different types of flat-field most commonly used in astronomy, as well as the removal of interference fringes visible in CCD images in the near infra-red. The second is a survey for old halo white dwarfs by searching for high proper motion objects in the comparison of two (I-band) data sets, observed 3 years apart. The code developed in the first part of this project, and all other operational parts of the OmegaCAM software are used in the data reduction necessary for this survey. The first half of this report deals with a new method to combine dome- and twilight flat-fields, while the second discusses the survey.

Chapter 1

Programming work for OmegaCAM

Part of the work I have done entails writing data reduction software within the OmegaCAM project. The work focuses on the flat-fielding and de-fringing step in the data reduction process. Most of the OmegaCAM software is written in the Python language. Python is a scripting language with Object Oriented Programming (OOP) as an integral basis. There are several external programs/libraries embedded in the pipeline, such as Eclipse (image manipulation), LDAC (astrometry), SExtractor (source extraction), and SWarp (image co-addition) which are written in C.

The code developed for this project is also written in the Python language and uses functionality from Numerical Python (NumPy), which is an extension written particularly to do operations on large arrays/matrices.

1.1 CCD data reduction in general, an introduction

Raw telescope data are not ready for scientific evaluation because they still require final calibration: the removal of instrument footprints. This calibration process can be split up into parts, as there are different physical processes that require day to day calibration.

1.1.1 Bias and Dark Current

The amplifier linked to each CCD chip in a telescope camera introduces a fairly stable 'static' signal, which might display a pattern across each chip. The signal is present in each image taken by the camera, of any exposure time. In fact it is even present when reading out the detector without exposing it at all. This so-called bias constitutes a constant for each pixel, that has to be subtracted from any image data.

The CCD driver electronics allows "reading-out" more pixels than are physically present on the CCD. This results in *prescan* and *overscan* regions on the output images that can be used to obtain a bias level. A disadvantage of using these is that only a general large scale structure of the bias can be derived by interpolating between the prescan and overscan values. Also, few pixels are available to base averages on. On the other hand, it is known that the bias level may vary by several ADU during a night and in this way the overscan regions allow the bias and science images to be determined at the same time, so these small variations in the bias level may be corrected for. Because the required number of bias images per night is limited (filters do not influence it) and the bias level is relatively stable, using bias exposures may be preferable, depending on the CCD. The exact procedure to calculate the bias in the pipeline is under investigation, based on the result of laboratory tests with the OmegaCAM detectors. An *overscan correction* will probably be used for the OmegaCAM data, but the current implementation uses bias images to correct any bias structure.

In uncooled cameras another source of bias can exist in the form of so-called dark current, which are electrons freed as a result of the temperature of the CCD chip itself. However, in detectors cooled with liquid nitrogen, that is, most (all?) current telescopes, this contribution is negligible. Dark current is measured as a current per unit time and hence has to be multiplied by exposure time before subtracting. In the case of OmegaCAM the dark current will be monitored, but it is assumed that it will be negligible.

1.1.2 Flat-fielding

Another necessary calibration step is flat-fielding. A flat-field, by definition is the response of the telescope and camera to a field of uniform radiation. Due to the different paths through the telescope that photons incident on different pixels of the detector have to take, they will be influenced in different ways. This translates into the collection of more or fewer photons per second at different places on the detector. Dust particles on the dewar (nitrogen cooled chamber) window, filters and detector (CCD) have a recognizable effect. The former create out-of-focus blobs or rings, while the latter create sharp artifacts of a few pixels in size. Finally each individual pixel has its own *quantum efficiency*; the efficiency with which incident photons result in trapped electrons. Flat-fields often display horizontal and vertical lines of higher sensitivity, these are a result of the production process of the CCD.

In practice there are two ways in which specific flat-fields are obtained. Dome flat-fields are created by pointing the telescope at a screen on the inside of the dome which is illuminated by lights. Twilight flat-fields are observed during morning or evening twilight, when it is bright enough that few stars contaminate the field and dark enough that the detector does not immediately saturate.

A flat-field can also be constructed from a collection of science images, preferably those with few stars and no extended objects like nearby galaxies. These images are combined while masking the sources in them. This can be done by median-averaging enough science images that are relatively uncrowded. For small cameras and telescopes it may be possible to find an almost completely blank area on the sky to point at and make dedicated sky flats but with the new generation of wide-field cameras like OmegaCAM this is impossible.

There are advantages and disadvantages of each type of flat-field. Dome flats are generally made in controlled conditions which means it is easy to reach ADUs (Analog to Digital Unit, or counts) in each pixel in the most linear part of the CCDs sensitivity curve. (About 20000 ADU in most cases.) The disadvantage of using dome flats is that the dome light(s) used to illuminate the screen of which the dome flats are taken create an inhomogeneous field, which means that the largest scale gain variation of the telescope and camera may not be correctly displayed. Furthermore, the colour of the dome lights is different from the colour of the night sky and the direction in which light enters the telescope may be different than during night time observations as well. Lastly, while it is easy to reach 20000 ADU in most filters using dome lights this may not be the case in the near-UV where many lamps produce little radiation. In the case of OmegaCAM lamps will be used which produce enough near-UV radiation.

The advantages of twilight flats are that the colour and uniformity of the twilight sky are a much better approximation to the circumstances during science observations than in the case of a dome flat. It is however difficult to obtain the right number of counts in a twilight flat, as the sky darkens or brightens quickly during twilight. Time is very limited and consequently, so is the number of twilight flats available in each filter band. Since averages are then based on fewer values the photon noise will be more important, and if the twilight flats have a low number of counts any noise produced during the read-out of the CCDs (*readout noise*) may be significant. Aside from this, in twilight flats taken near the end of evening twilight stars will be visible, which means a sufficient number of twilight flats at different pointings is necessary to remove the stars. A final problem is that fringes may be present in the twilight flats. (see section "Fringes")

The above-mentioned characteristics of dome flats and twilight flats indicate that twilight flats are better suited to remove the large scale instrument footprints, while dome flats are more suited to describe small scale gain variations (dust etc.) These considerations result in the desire to combine dome flats and twilight flats, as well as the night sky flats (also named superflats) in what is known as a master flat-field.

1.1.3 Bad pixels

Damage or faults on a CCD can result in small areas or single pixels that have incorrect values. Some pixels do not collect any charge when illuminated and hence are dark in every exposure (cold pixels). Some pixels have a very high dark current and hence are bright in every exposure (hot pixels). As CCD chips are read out, the charges in each row of pixels are transferred towards the adjacent row and the row at the edge is read. The result of this is that a single pixel that has a very low *charge transfer efficiency* (CTE) will influence the flow of charge from all the pixels behind it, resulting in a bad column in the image.

Bad pixels show up at the same pixel position in every image, and they are usually marked in mask/flag frames and assigned a weight of zero in further reduction.

1.1.4 Fringes

In exposures of (backward illuminated, thinned-) CCD detectors while using broad-band, near infra-red filters or appropriate narrow band filters, "fringes" may be visible. These look like the structures seen in oil as it reflects light (thin film interference). Photons incident on a backward illuminated CCD detector enter a silicon layer where they liberate electrons, which are trapped by the pixel structures. In these CCDs, to photons of sufficiently low energy (near infra-red) the silicon layer can have an optical depth of more than twice the thickness of the silicon layer. When this is the case photons that reflect in the CCD can interfere with those incident on it, leading to an interference pattern across the chip, the shape of which depends on variations in the thickness of the silicon layer and the nature of the incident light.

It is known that in the case of these broad band filters, where normally any fringing would be invisible against the background of broad band radiation, the cause of fringes lies in the distinct atmospheric emission lines of some molecules and ions in the near-infrared (mostly OH and O_2). The fringe pattern and its stability, particularly the amplitude of the fringes across the CCD, varies from (telescope-) site to site and no satisfactory models for their behaviour exist. The amplitude of the fringes can be up to about 10% of the sky background.

The nasty aspect of fringes is that they are an additive error like the bias, but that they are only seen combined with the flat-field response, which is a multiplicative error. This makes the separation difficult. Fringes are structures on the scale of several arcseconds, (dozens of pixels in the case of WFI), at least in the direction across the fringes, which means they are hard to computationally distinguish from stars, and source extraction programs can hence deliver unreliable results.

1.2 Overview of the OmegaCAM calibration pipeline

Below (Figure 1.1) is a figure detailing the various *requirements*, *sequence files* and *calibration files* defined in the OmegaCAM User Requirements Document (URD). The figure displays the required software parts and intended data flow through the pipeline, from on-site quality checks, to catalog/database data.

1.2.1 Object Oriented Programming

Because the pipeline software is constructed in an object oriented style, *classes* are associated with the various conventional calibration images. For example,

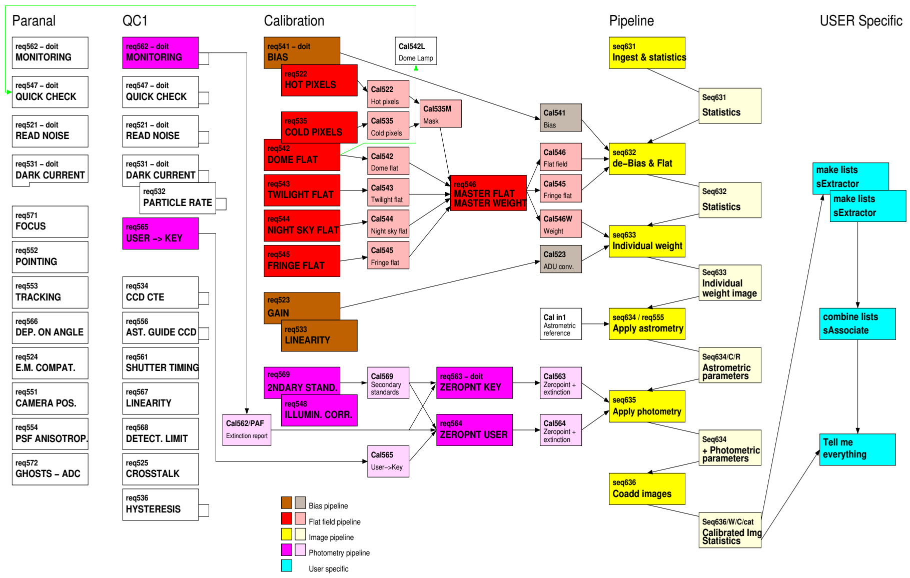

Figure 1.1: OmegaCAM data-flow model

bias exposures become *instances* of the RawBiasFrame class, and twilight flats become instances of the RawTwilightFlatFrame class. These instances of classes are the 'objects' of OOP. Classes may have incorporated *attributes* and *methods*. Methods perform a task on the object they belong to while attributes are properties such as constants, flags or links to other objects, that may be needed by methods.

Various recipes have been coded that control the creation of instances of these classes. There may be different ways to create an instance (object) from a class, depending on which attributes are set to what values, and which methods are used. A ColdPixelFrame object for example can be created by using a DomeFlatFrame or a TwilightFlatFrame object as input.

Within the object oriented programming style *inheritance* is an important concept. Classes can inherit attributes and methods from other classes. This facilitates the re-use of code. In the above example, the ColdPixelFrame class has an attribute 'flat', which must be an object of the BaseFlatFrame class; DomeFlatFrames and TwilightFlatFrames (these are master dome- and twilight images, which are explained in the next sections) inherit from the BaseFlat-Frame class and hence are both allowed as input.

In Figure 1.2 is a more detailed view of the calibration and image pipelines. The larger boxes in the calibration pipeline have recipes associated with them that produce calibration files, often in FITS format. These files are denoted by the smaller boxes. The classes associated with the calibration files are given in italic.

It has to be mentioned that the entire OmegaCAM pipeline is run on a per-chip basis; every CCD is reduced totally independently from all the others. This way parallel processing of the 32 CCDs that will be present in the camera becomes possible, greatly speeding up the data reduction. For each individual CCD the following ("standard", used in this project) calibration files are created in the Bias- and Flat-field pipeline (see the black outlined region in 1.2):

master bias (Cal541)

The master bias is made by combining a number of raw bias images. The images are stacked and an average is calculated. The result is stored in FITS format, like most of the cal files in the calibration pipeline.

hot pixels (Cal522)

A master bias image is used to detect hot pixels. The mean, median and standard deviation of the background are estimated by iteratively excluding outlying pixels. Pixels more than 5σ above this mean are considered hot pixels.

cold pixels (Cal535)

A master dome flat or master twilight flat is used to detect cold pixels. This is done by estimating a background in the flat-field (using SExtractor). The flat is flat-fielded by dividing through its background. Pixels deviating more than 5% from the the mean are considered cold pixels.

master dome flat (Cal542)

Raw dome flat images are combined into a master dome flat. The reason for this is the reduction in (relative) noise, which scales with a factor of $1/\sqrt{N}$, where N is the number of frames used, that can be achieved. These raw dome flats are trimmed (the overscan and prescan regions are cut away). Subsequently the master bias image is subtracted and the resulting images are normalized (the mean pixel value is set to 1.0). Cold pixel maps and hot pixel maps are used to exclude any bad pixel values from the normalization. These normalized dome flats are stacked in a cube and an average is calculated: the master dome flat.

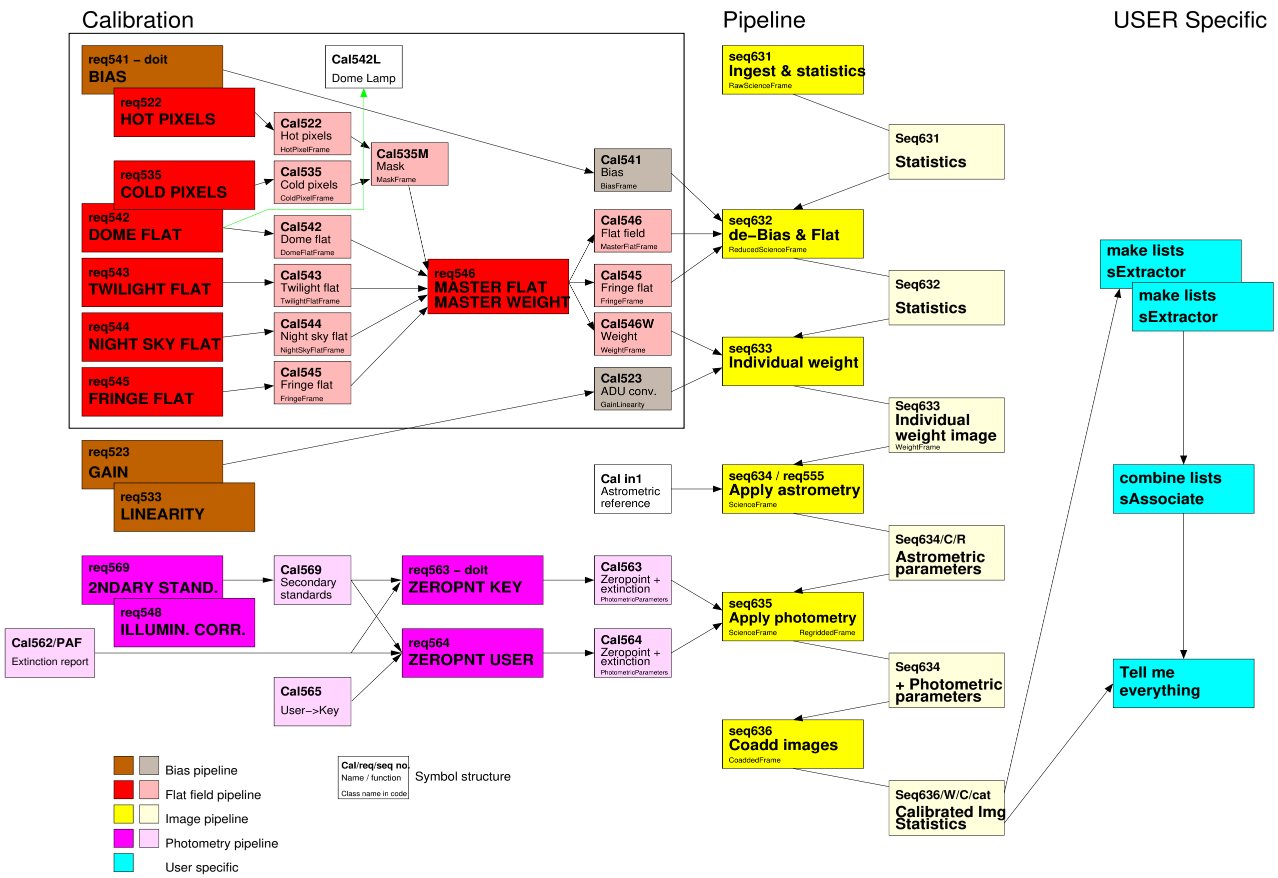

Figure 1.2: Calibration and image pipelines with classes. The black-outlined area is the most relevant to this work.

master twilight flat (Cal543)

Like in the case of the master dome flat a master twilight flat is constructed from a series of normalized raw twilight flats. In this case however a median average is calculated from a cube of twilight flats. This is done because stars may be present in twilight flats, and the median is much more efficient than the mean in eliminating outlying pixel values, it is less efficient in reducing noise however.

night sky flat (Cal544)

The code for this requirement has not been implemented yet.

fringe flat (Cal545)

See section 1.4.

master flat (Cal546)

See the next section.

1.3 Constructing the master flat-field

As discussed earlier, dome flats will generally have better controlled counts per pixel, while they do not display fringes (in the case of broad band filters), but the illumination and colour of the lamps used is not very good. Therefore small scale structures in the dome flats are relatively well described, while the large scale structure is not. Twilight flats have a relatively good source of illumination and colour but often highly variable counts which means Poisson- and readout-noise are a larger factor.

Hence, in the construction of the master flat, high spatial frequency components are extracted from the dome flat and low spatial frequency components from the twilight flat.

In order to make a master flat-field, different spatial frequency components are extracted from the master dome flat and master twilight flat. The process is explained below.

1.3.1 The Fourier Transform

In order to extract different spatial frequencies from the master dome and master twilight flats, the Fourier transform is used. The Fourier transform in two-dimensions is given by:

$$F(u,v) = \int_{-\infty}^{\infty}\int_{-\infty}^{\infty} f(x,y)e^{-i2\pi(ux+vy)}dxdy \tag{1.1}$$

Since we are dealing with pixel images there are values available only at discrete intervals of space, and for a limited amount of space. Hence the discrete Fourier transform is necessary. It is given by the following formula (Bracewell 1965):

$$F(\mu,\nu) = M^{-1}N^{-1}\sum_{\sigma=0}^{M-1}\sum_{\tau=0}^{N-1} f(\sigma,\tau)e^{-i2\pi(\mu\sigma/M+\nu\tau/N)} \tag{1.2}$$

where the integers σ and τ may be connected with the (x,y)-plane as follows. If the sampling intervals are X and Y, and x_{min} and y_{min} are the minimum values of x and y to be considered, then

$$\sigma = \frac{x - x_{min}}{X}$$

$$\tau = \frac{y - y_{min}}{Y}$$

Fast Fourier transforms (FFTs) calculate the discrete Fourier transform (originally only for arrays of size 2^N), in a fast way, so that for an array of size N, the required number of operations scales with N log N rather than N^2.

The discrete Fourier transform assumes that outside the given range (say 0 to N-1 for one dimension) the series is extended N-periodic.

An external FFT is used in the process of constructing a master flat, namely FFTW ("Fastest Fourier Transform in the West"). This library is written in C and has been made available for NumPy applications. The reason why we use it is that the FFT included in NumPy proved inconsistent with the documentation, and FFTW is also considerably faster. This transform can calculate multidimensional transforms of arbitrary size arrays.

By transforming images to Fourier space and filtering it is possible to extract different (spatial) frequencies from an image. Such a technique is used here to construct the master flat.

In order to perform Fourier filtering a function was written in Python/NumPy to create a two-dimensional array that contains the values of a two-dimensional Gaussian function. This array and the shape of the Gaussian depend on the shape of the input images because the shape of the input image is conserved by the Fourier transform.

Fourier filters fall broadly into three categories, low pass filters, high pass filters and band pass filters. Low pass filters remove high frequencies and high pass filters remove low frequencies, while band pass filters transmit a range of frequencies. A Gaussian low pass filter has a smoothing effect; it removes high spatial requencies.

The Fourier filter is applied in Fourier space, so we try to get a feeling for the width of the convolution kernel in image space that is the equivalent of this filter. Therefore calculate the FWHM of the inverse Fourier transform of a statistical two-dimensional Gaussian in Fourier space (which is also a Gauss).

We need the inverse discrete Fourier transform (inverse of Eq. 2):

$$f(\sigma,\tau)=\sum_{\mu=0}^{N-1}\sum_{\nu=0}^{M-1}F(\mu,\nu)e^{i2\pi(\frac{\sigma\mu}{N}+\frac{\tau\nu}{M})} \tag{1.3}$$

Here F is our Gaussian, G:

$$G(\mu,\nu)=e^{-(\frac{\mu^2}{2\sigma_\mu^2}+\frac{\nu^2}{2\sigma_\nu^2})} \tag{1.4}$$

In order to calculate the sum assume we are dealing with a continuous function after all and calculate the integral equivalent of the summation:

$$f(\sigma,\tau)=\int d\mu\int d\nu e^{-(\frac{\mu^2}{2w_\mu^2}+\frac{\nu^2}{2w_\nu^2})}e^{i2\pi(\frac{\sigma\mu}{N}+\frac{\tau\nu}{M})} \tag{1.5}$$

This integral can be split in a part for μ and ν. Under the transformations:

$$r=\frac{\mu}{\sqrt{2\pi}w_\mu} \qquad s=\frac{\nu}{\sqrt{2\pi}w_\nu}$$

the integrals give the following result:

$$f(\sigma,\tau)=\sqrt{2\pi}w_\mu e^{-2\pi^2\frac{\sigma^2}{N^2}}\sqrt{2\pi}w_\nu e^{-2\pi^2 w_\nu^2\frac{\tau^2}{M^2}} \tag{1.6}$$

This is an equation for a two-dimensional Gaussian function with statistical widths:

$$w_\sigma=\frac{N}{2\pi w_\mu} \qquad w_\tau=\frac{M}{2\pi w_\nu}$$

The FWHM of a Gauss relates to its statistical width as:

$$2\sqrt{2\log 2}\sigma=2.3548\sigma$$

In most current wide field imagers EEV 2k×4k CCD chips are used. This means N≈2000 (NAXIS1) and M≈4000 (NAXIS2). The FWHM in the NAXIS1 direction is then $\approx 750/\sigma$. A default value of 9 for the σ of the filtering Gauss is chosen. This results in convolution on the scale of $\sim$ 83 pixels.

As a result of the smoothing effect of the low pass Fourier filter bad pixels have an effect on neighbouring pixels when it is applied. Especially in the case of structures on the scale of about 10-20 pixels this results in smeared out structures. This can be avoided by using the cold and hot pixel map and first replacing the bad pixels. Bad pixels are replaced by the median value of a box of 37×37 pixels, surrounding the bad pixel.

Because of the assumed periodicity of the Discrete Fourier Transform in the case of flat-fields edge effects occur. At the edges of the image, say pixel [N, m], the Fourier transform assumes the next pixel has the value of pixel [1, m]. The result is that the transform calculates pixel values near the edges that incorporate values at the opposite edge, and this leads to darkening on the bright side and brightening on the dark side if there is such a gradient in the flat-field. To counteract this problem the edges are mirrored and the Fourier transform is calculated over the larger array.

1.3.2 Combining the components

When the large scale structure is extracted from the twilight flat and the small scale structure from the master dome flat, the two components are normalized (divided by the mean, excluding bad pixel values) and multiplied to give the master flat. In short the construction of the master flat can be described as follows:

$$M[i,j] = \frac{D[i,j]}{Conv(D[i,j])} Conv(T[i,j]) \tag{1.7}$$

where M is the master flat, D the master dome flat and T the master twilight flat. *Conv* is the convolution procedure described in the previous section.

1.4 Constructing fringe maps

Fringe maps are constructed from a set of partially reduced science frames. After trimming, de-biasing and flat-fielding an image it is assumed any remaining systematic effects (i.e. aside from the astronomical objects) are either bad pixels or fringes. In order to create a fringe map that can be used to correct all images taken through the same filter during a night, a set of science images is reduced and normalized. These images are placed in a cube and a median average is calculated. The median average corrects very well for any outlying values, so any stars, cosmic ray events or satellite tracks are removed, at least when sufficient images are provided to base the median average on (~ 10). Care should be taken to avoid using images of extended objects, such as nearby galaxies, or multiple exposures at the same pointing. In the case of WFI data, when fewer than about seven images are used, residual features from bright-star halos (reflections) can be seen.

The construction of the partially reduced science frames can be described as follows:

$$RS = \frac{trim(R) - B}{F} \tag{1.8}$$

$$RS = \frac{RS}{median(RS)} \tag{1.9}$$

where RS is the partially reduced science frame, R the RawScienceFrame object, B the BiasFrame object (the master bias) and F the MasterFlatFrame object. In the above formulas *trim* cuts away pre- and overscan regions, and *median* is a median determined by iteratively excluding outlying pixels in the image.
The construction of the FringeFrame can then be described as:

$$Fr = norm(median(C)) - 1.0 \tag{1.10}$$

where C is the cube of partially reduced science frames. The normalization excludes bad pixels as defined by the mask. The median is the median through the depth of the cube. Bad pixels are assigned a value of 0 in the FringeFrame.

1.4.1 Scaling fringe maps

During a night the brightness of the sky will change, especially near evening and morning twilight. The result of this is that the strength of the emission lines that cause fringes w.r.t. the sky changes, and hence the amplitude of the observed fringes. Therefore fringe maps should be scaled to fit the amplitude of the fringes in each science frame. A simple automatic scaling algorithm was made to perform this task.

It is assumed that the standard deviation in a science image that displays fringes depends on the amplitude of the fringes. Much too low or much too high scale factors result in a higher standard deviation than the right scale factor. Curves can be made of the relation between the fringe map scale factor and the standard deviation in the resulting reduced science image (see figure 1.3). Each curve shows one clear minimum, that is determined by an iterative algorithm.

The standard deviation is calculated from all non-bad pixels that have values within a given threshold from the median background level. When using the entire image to calculate the standard deviation, the scale factor required to best eliminate the fringe pattern is generally underestimated. Selecting an area of strong fringing to derive a scale factor gives better results (K. Meisenheimer, private communication). In that case however the results might be influenced by the presence of stars in these regions. Possibly a good alternative is to use a mask indicating the location of the maxima and minima of the fringe pattern as a function of pixel position, which are considered to be stable.

The described FringeFrame routine is very similar to conventional night sky flat (superflat) procedures. This was anticipated and hence the procedure to make fringe maps may be used in the NightSkyFlatFrame class. From a preliminary study of the quality of the flat-fielding procedure (in particular the quality of twilight flats for WFI) it appears desirable to use a superflat.

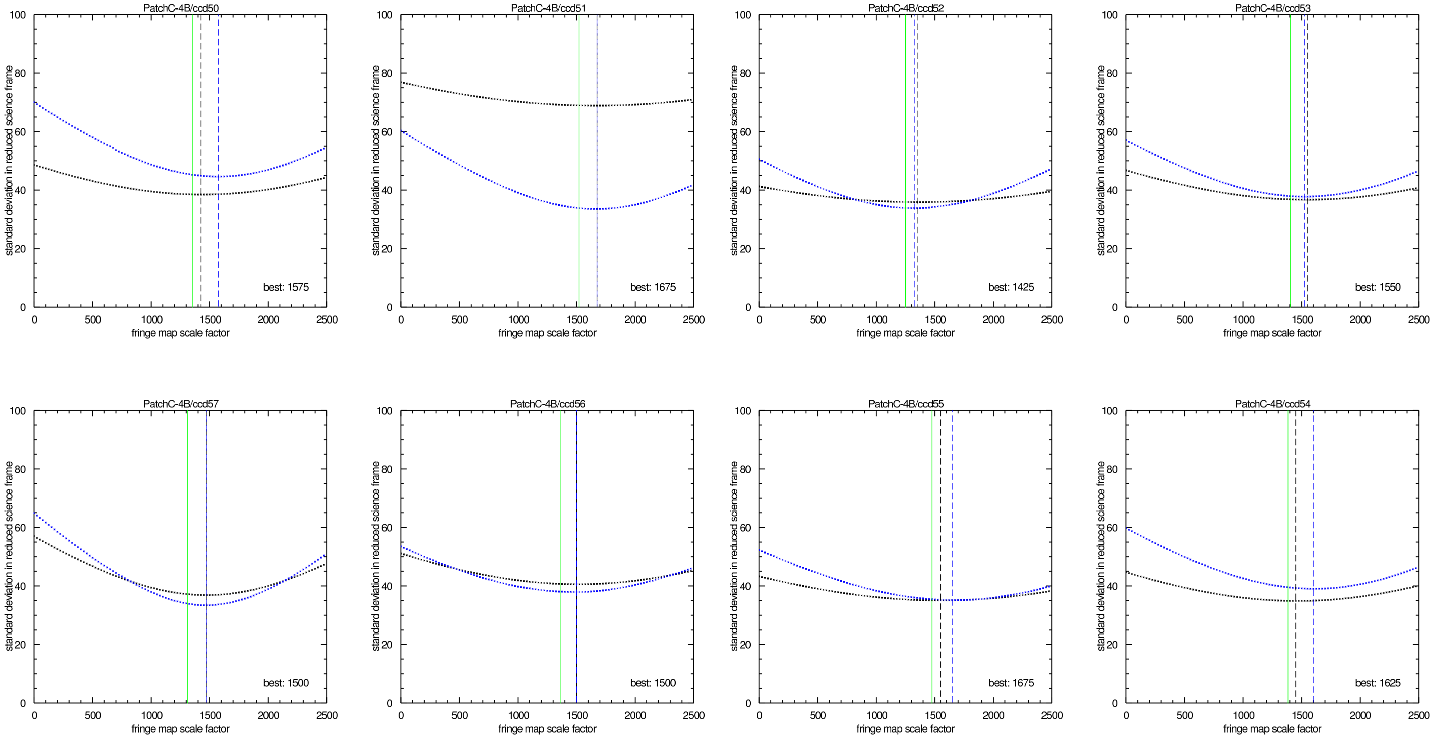

Figure 1.3: Standard deviation in the calibrated science image vs. fringe map scale factor, for each CCD of the WFI detector. Two curves are displayed, one using the total image (black), the other (blue) using areas of large fringe amplitude, which differ depending on the CCD of the WFI detector. The green line is the median sky background in the science image.

Chapter 2

A proper motion survey for halo white dwarfs

2.1 An introduction to the dark matter problem of the Milky Way

In the early twentieth century a by now longstanding and fundamental problem in astronomy surfaced. This is the problem of the apparent existence of large quantities of unseen matter in the Milky Way, the exact nature of which is still unknown. The existence of this so-called dark matter is inferred from measurements of the dynamics of the Milky Way, in particular the rotation speed of stars as a function of distance from the center of the Milky Way and the velocity dispersion of stars in its central region. The rotation speeds of stars and the dispersion in their speeds in the bulge indicate more mass exists than what the total amount of visible stars, gas, dust and other objects adds up to.

Various forms of matter can theoretically account for this 'missing mass'. Among them are massive compact halo objects (MACHOs) such as the remains of old stars that have blown their outer layers into space at the end of their lives (white dwarfs) or stars so light that they at best only briefly burn some hydrogen, but remain cold and dark afterwards (brown dwarfs). More exotic MACHOs such as black holes and neutron stars have also been proposed. These objects have in common that they are either very faint or have colours which made typical star count surveys insensitive to them, and hence they may have escaped detection.

Aside from MACHOs different explanations to the problem have been proposed. Several projects in the field of theoretical physics have striven to detect neutrinos. Neutrinos are very elusive elementary particles that are produced in massive quantities in stars but almost never interact with other particles. In the past few years indications have been uncovered that neutrinos have in fact a finite mass, and because they are formed in such high numbers this mass may add up to astronomically significant amounts. On theoretical grounds the existence of 'exotic matter', massive particles that only weakly interact with their surroundings (WIMPs) can also be derived.

A more conventional explanation may be that large quantities of gas and dust exist in the Milky Way that are currently unaccounted for.

In the last five years the debate about the nature of the dark matter in our galaxy and in particular whether it exists in the form of MACHOs has intensified as the results of several surveys into this matter were published (Alcock et al. (2000) (microlensing survey), Ibata et al. (2000) (proper motion survey), Oppenheimer et al. (2001) (proper motion survey)). None of these surveys have gone uncriticised however.

2.1.1 Microlensing surveys

Microlensing surveys search for brightening and subsequent darkening of background stars due to the lensing effect of some foreground gravitational well as it passes in front of the star. In order to find a few of these events, millions of stars in the Large Magellanic Cloud and Small Magellanic Cloud were observed by the EROS and MACHO collaborations. This effort resulted in a few dozen microlensing events towards these galaxies.

These results formed the starting point of the ongoing controversy about the mass fraction of the galactic halo that MACHOs can conceivably make up, and the exact type of objects these MACHOs are. The authors claim that as much as 50% of the dark matter halo can consist of MACHOs of mass range 0.1-1.0$M_{\odot}$. This result strongly indicates brown, sub-, or white dwarfs as the predominant form of dark matter in our galaxy because they are the only known astronomical objects which can have these properties.

The conclusions of Alcock et al. (2000) and EROS, have been challenged however, with claims that the observed microlensing events can also be explained by lensing due to lenses inside the LMC itself (R. Di Stefano 2000).

2.1.2 Proper motion surveys

Stars in the Milky Way can display an annual movement on the sky. There are several possible causes for such a motion. One of them is parallax, which is caused by the changing angles of projection as the Earth orbits the sun. Parallax is only measurable for very nearby stars. "Proper motion", is caused by actual space motion of stars w.r.t. the LSR.

The Hubble Deep Field (HDF) images have become a source of information about halo white dwarfs. Ibata et al. have used the initial HDF images as the first epoch of an extremely deep proper motion survey with a one year baseline. (Which was later extended to a two-year baseline.) In that survey the authors report the discovery of up to 5 very faint, blue objects; possible halo white dwarf candidates. Two of these sources displayed a visible proper motion of 23$\pm$5 and 26$\pm$5 mas yr^{-1}. After a third epoch set of observations however, the claims to the detection of these halo white dwarfs were dropped, as the proper motions could not be confirmed by the new observations.

A property of these HDF observations is that they are very deep, to limiting magnitudes of I and V ∼28, while the total area covered is extremely small (0.0015 square degrees). Other surveys claim they can be more effective by covering much larger areas while not probing as deeply. The observations done for the purpose of this project are an example of such a survey.

2.2 The observations

The proper motion survey performed for this project is based on data from the ESO Imaging Survey (Benoist et al. 1999) and our own observations obtained with the Wide Field Imager on ESO's MPI-2.2m telescope. In February of 2001, during three nights EIS-WIDE patches C and D were re-observed in the I-band, in three separate exposures of 10 minutes time each. The EIS-WIDE C and D patches were originally observed with ESO's NTT (EMMI) telescope from November 1997 through march 1998 and hence the survey has a baseline of 3 years. Patches C and D each span 6 square degrees of the sky. The EIS data consists of 150 sec. exposures; each patch is covered by a mosaic of 600 partly overlapping fields such that each position is covered twice. Note that the data provided by ESO are the individual calibrated images and catalogs, and not the coadded images. The total area covered by both data sets is ∼10.5 square degrees.

Together with the depth attainable with the three separate 600 sec. WFI exposures, our own observations were estimated to probe the halo luminosity function down to absolute magnitudes of $M_I \sim 18$. This translates to probing white dwarfs with cooling ages as high as 16 Gyr.

2.3 Data reduction

The first step of the data reduction process, the construction of the necessary calibration files is described in part I of this report. This section will focus on the data reduction starting with the astrometric and photometric calibration and the extraction of sources from the calibrated images.

Both the first epoch observations by EIS and the second epoch observations by WFI were astrometrically calibrated by using the USNO 2.0 catalog as reference. Originally, the EIS data were calibrated with an older version of the US Naval Observatory catalog and an offset between the two was evident. In order to reach the highest signal to noise ratio for each data set these astrometrically calibrated exposures were coadded. This task is performed by SWarp (Bertin 2002). The EIS data were coadded in large fields covering 1/4th of each Patch (∼1.5 square degrees). Each of these fields then cover 6 WFI pointings. To get a measure of the quality of the astrometry, plots can be made such as figure 2.1. Here the differences in position between sources from the EIS catalog and the

WFI catalog for one WFI field are given.

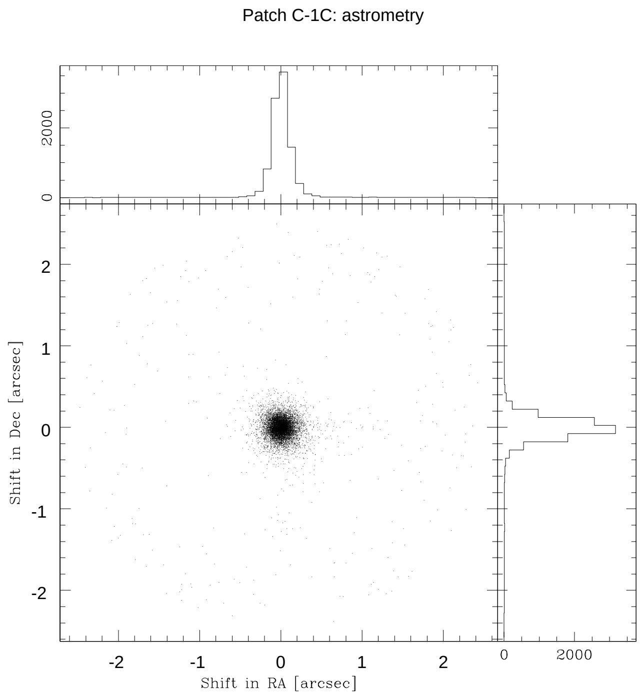

Figure 2.1: Differences in RA and Dec of sources associated within 2.5 arcsec. There is an excess compared to normal Gaussian behaviour which is apparent near offsets of 2 arcsec. This is due to inaccuracy of the astrometry near the edges of the WFI CCDs.

Photometric calibration was done using the information in the EIS catalogs of the individual EIS images (i.e. $\sim$600 per patch). The provided EIS images were all background subtracted and all have the same photometric zero point, so this zero point can be applied to the coadded data as well to calibrate them. A check of the process is displayed in figure 2.2.

From figure 2.2 it is assumed the coadded image catalogs can be calibrated by using the zero point provided by the calibrated EIS data. Note that the EIS images are very small compared to the coadded image, and that each point on the sky is sampled (at least) twice by the EIS data. The difference is slightly larger than zero on average. This is an effect of the bilinear interpolation of neighbouring pixels when images are resampled during coaddition. The spread for bright (saturated) sources is explained by possibly different saturation levels, due to differences in seeing and sky background, of the contributing images. The spread at the faint end is explained by the less accurate photometry possible

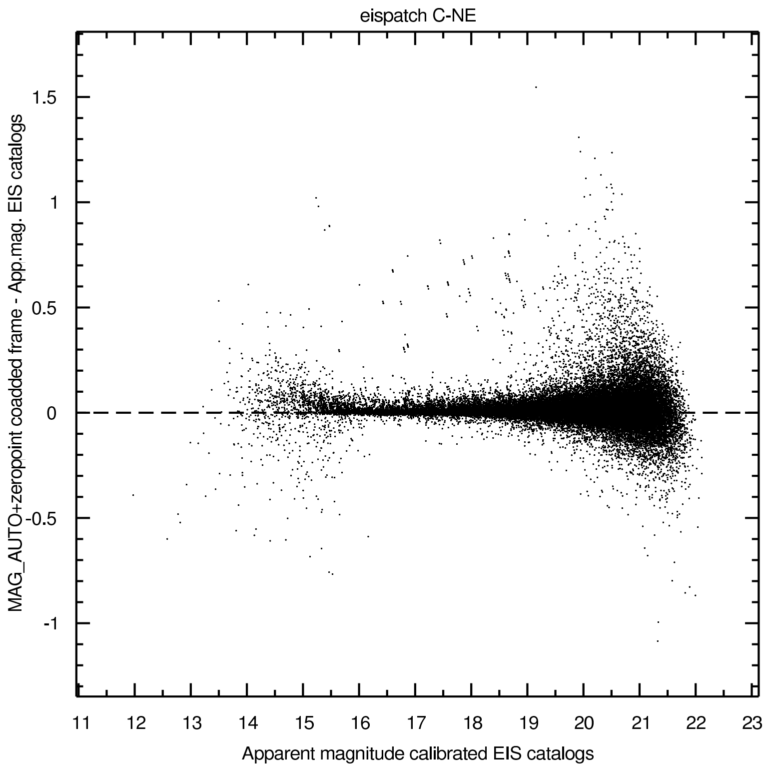

Figure 2.2: Relative magnitude calibration I. Magnitude comparison of coadded image catalogs and calibrated EIS catalogs. The coadded image catalog magnitudes have been corrected with the zero point stated in the individual EIS image headers.

near the (brighter) detection limit of the individual frames as compared to the coadded images. Some of the individual EIS images have certain pixels masked out, while others have not; especially the sources between $m_I = 16$ and $m_I = 19$ are affected by this.

Using the calibrated coadded image catalogs, the WFI data can be calibrated. Since the OmegaCAM pipeline treats the WFI chips completely independently there is an extra step to take care of the difference between the individual chips. For each pointing in the WFI data an association was performed with the relevant EIS field to find the stationary objects. (See the next sections and Appendix B.) For each WFI pointing a least squares fit is made to the Kron elliptical aperture magnitudes as a function of the same parameter for the coadded EIS data. (See figure 2.3.)

Source extraction was performed on the coadded data sets using SExtractor (Bertin and Arnouts 1996). There are almost no extended objects in the fields. This allows the use of sensitive deblending. SExtractor calculates a large number of quantities for each of the detected objects. Relevant quantities are explained in Appendix A.

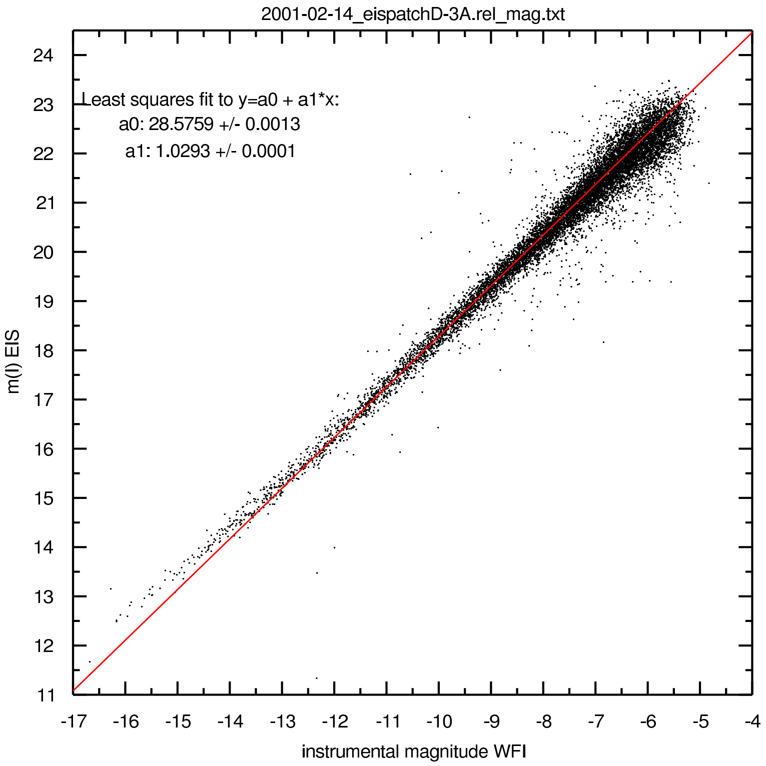

Figure 2.3: Relative magnitude calibration II. Magnitude calibration of WFI data using the EIS coadded image catalogs. Note the effect of saturation for WFI mag < ∼-12.5. The fit is to points of -12.5 < mag WFI < -7.5

2.4 Associating catalogs

In order to find moving objects in the data set the catalogs of extracted sources are associated. This is done using the Leiden Data Analysis Center (LDAC) software, developed for the DENIS survey (Deul 1993), see Appendix B.

The adopted strategy is to first find all good matches (the stationary objects) between the catalogs. These are then excluded from both catalogs, resulting in catalogs of unmatched objects. These objects are matched with each other to find any possible counterparts closer than a given search radius. Such matches are possible high proper motion stars. Objects are considered stationary if the shift between the barycenters is smaller than 0.60 arcsec over the baseline of 3 years. Objects in the catalogs of unmatched sources are matched with counterparts within 15.0 arcsec. The survey is therefore sensitive to proper motions of $0.2 \leq \mu[''/yr] \leq 5.0$.

In short the following selections are performed on the catalogued objects (explained in more detail below):

1. minimum half-light radius: 1.1 pixels (exclude cosmic rays/bad pixels)
2. maximum half-light radius: 5.0 pixels (exclude extended sources)
3. SExtractor flags: 1, >8 excluded
4. magnitude < detection limit
5. magnitude difference between matches < 1.0
6. weight maps $\neq 0$
7. distance to bright stars >50"

half-light radii

The first four selections are performed after the exclusion of the "stationary" objects from the catalogs. The last three are performed after the proper motion candidates have been determined. N. Kaiser (1995) used half-light radius vs. magnitude plots to separate "moderately bright" stars from galaxies. Such a plot can also be used to exclude detections on cosmic rays and what appear to be leftover hot pixels. (See figure 2.4.) A clump of objects with small (smaller than the seeing) half-light radius is clearly visible. As a first step these are excluded from the input catalogs. Objects with half-light radius larger than 5.0 pixels are also excluded; it is assumed these are galaxies.

SExtractor flags

Objects with SExtractor flags equal to 1 (bad pixels constitute more than 10% of the integrated area) and flags larger than 8 (problems with the object's isophotal or aperture data, which is related to image borders/bad pixels) are excluded because the position determination of such objects is inaccurate. Note that this selection is not the same as the check using the weight maps explained below.

detection limit

For each WFI field consisting of three consecutive exposures, histograms of the magnitude of objects are created. From these a detection limit is determined. Subsequently, all objects fainter than the brightest detection limit are excluded from both catalogs before the second association step. (See figure 2.5.) The steep drop in number counts near instrumental magnitude 22.0 is associated with the detection limit (R. A. Knox 1999). The coadded EIS data are often $\sim$0.5 magnitude deeper than the WFI data; the detection limits change from WFI field to WFI field (from $\sim$21.0 to $\sim$22.0), probably because the moon was

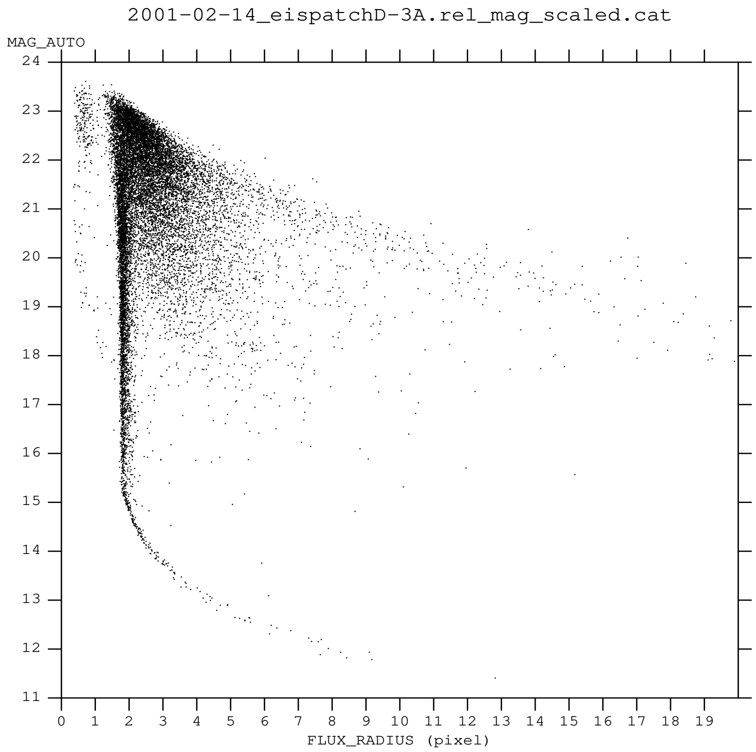

Figure 2.4: Magnitude-half-light radius plot for one WFI field. Points in the vertical bar with the turnoff near m_I=15 are stars; the turnoff is caused by saturation. Galaxies have larger half-light radii for equal magnitudes.

visible (between 49% and 70% illuminated) during large parts of the three nights of WFI observations.

relative magnitudes

In the cases of interest for the purpose of this survey, the matches have to be the same object. Therefore a selection based on the magnitude difference of each pair of objects can be done. Figure 2.6 is a histogram of the magnitude difference of pairs of objects associated in a search radius of 5.0 arcsec. Based on these histograms a maximum magnitude difference of 1.0 mag is set for possible candidates.

weight maps

For each coadded field weight maps were constructed. For each matched pair a check was performed whether either of the objects are located in a region where the weight maps are zero. For a cluster of 10×10 pixels at each object position

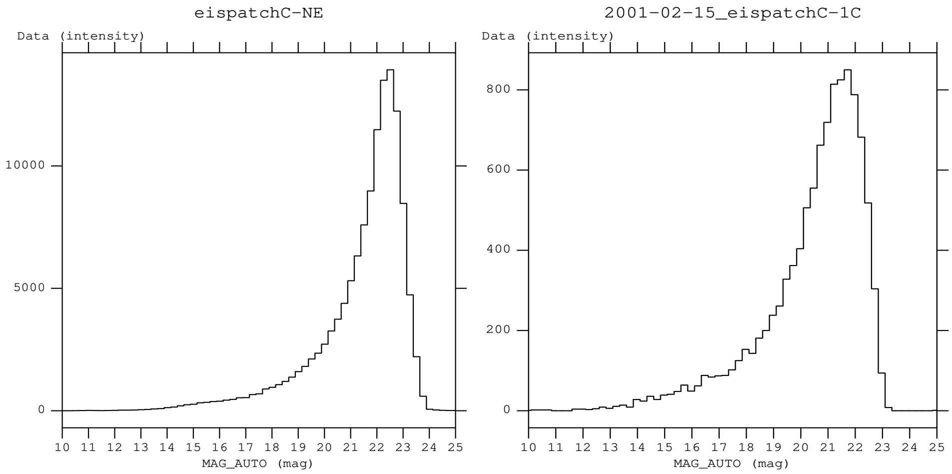

Figure 2.5: Histograms of an overlapping field, indicating the relative detection limits for EIS (left) and WFI (right) data.

statistics were determined. Pairs were excluded if for one or both of the objects the median of these pixels in either weight map was zero.

At this point there are still a large amount of (false) matches left. These can be attributed to several causes:

- bright stars
- image borders/gaps
- inaccuracy of the astrometry near the edges of WFI fields
- differences in deblending
- detections on cosmic rays

bright stars

Regions of radius 50" (approximately the extend of the brightest reflection that can be distinguished) near those stars with significant halos in the WFI images ($m_I < 10.5$) are excluded, since there are a large number of spurious SExtractor detections here. Unfortunately many of the bright stars have in fact two or three halos, the edges of which cause SExtractor to produce false detections considerably farther away. Some of the brightest stars are also not detected by SExtractor and some are located just outside the image so that only a halo is visible.

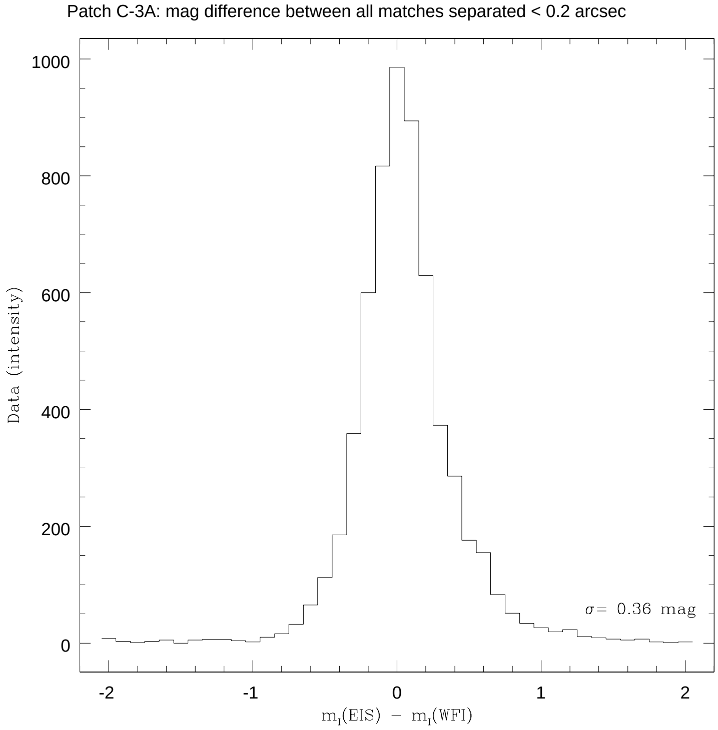

Figure 2.6: Magnitude differences across catalogs of all objects separated by less than 0.2 arcsec.

image borders

The coadded images that are compared always are a large EIS field and a smaller WFI field. In addition the three exposures that combine to make the WFI fields are not dithered. Therefore a large amount of unmatched EIS sources are available near the image borders and gaps in the WFI detector mozaic, and hence more false proper motion candidates are found in these regions. The weight maps of both coadded images are used to exclude matches where one of the sources is located in a masked or unobserved area of either image.

astrometry

There is an inaccuracy in the astrometry near the edges of WFI fields. See figure 2.7.

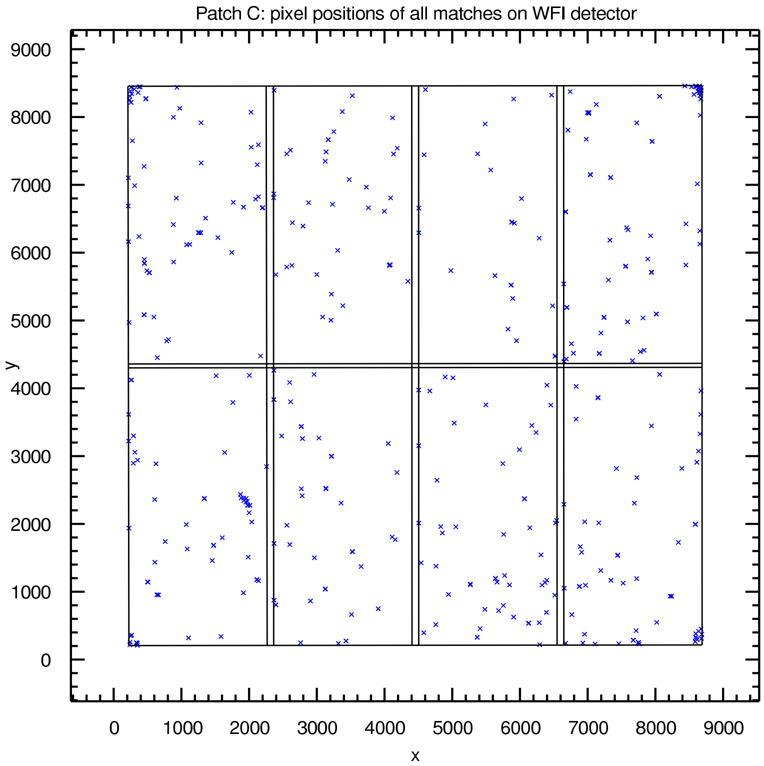

Figure 2.7: Location of all candidates in Patch C on the WFI detector. The solution of the astrometry can deviate substantially near the edges and in particular the corners of the WFI CCDs.

deblending

It is possible for two sources not to be deblended in one catalog while they are deblended in the other. This often results in two false proper motion candidates as the average position of the undeblended source is shifted w.r.t. each deblended source from the other catalog.

cosmic rays

In the calibrated EIS data a large number of cosmic rays are still present. These presumed cosmic rays are however not saturated in the coadded images. (Due to coaddition they are the average of normal and saturated pixels.) Even though a selection is done on half-light radius, there still are a number of cosmic rays that are not excluded. These may also result in false matches.

For each of the resulting matches ($\sim$1000), cutouts were made of the relevant regions in both the WFI and EIS data. These cutouts were blinked as a final check. The vast majority of objects are still false candidates.

2.5 Results

Three proper motion objects were detected. The objects are all of similar magnitude ($m_I \sim 15$). The New Luyten Two Tenths of an arcsecond catalog (Luyten 1979) was checked to see if these objects were already known.

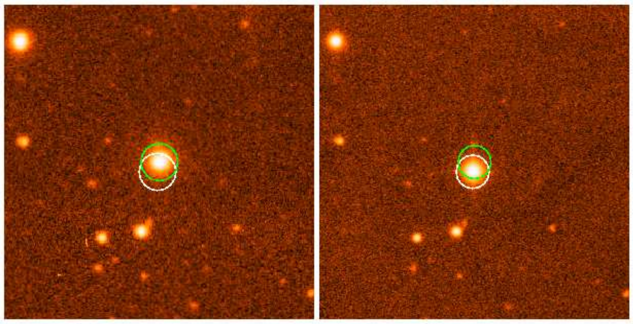

Figure 2.8: Candidate 1: this object is located in patch C and has an apparent I magnitude of 15.3. It has a proper motion $\mu = 0.76''/yr$. This object is known from the USNO B1.0 and 2MASS catalogs.

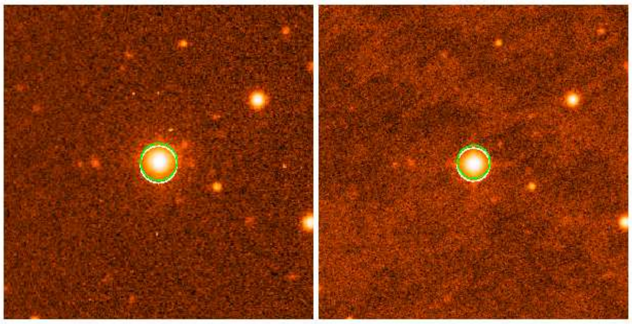

Figure 2.9: Candidate 2: this object is located in patch C and has an apparent I magnitude of 14.5. It has a proper motion $\mu = 0.21''/yr$. This object is a known proper motion object from the NLTT: 837-8.

From the NLTT catalog there are 5 known proper motion objects in patch C that also lie in the WFI data. Three of those are very bright stars that are saturated. (Two of these have halos in the WFI images.) One of them is candidate 2, and another object was excluded because it lies close to an image border where the astrometry is bad.

In patch D there are 6 known NLTT objects. Of these objects one falls below our (and actually NLTT's own) proper motion sensitivity limits, 3 are saturated (of which two are excluded because they have halos), one was excluded because of edge effects and the last one is candidate 3.

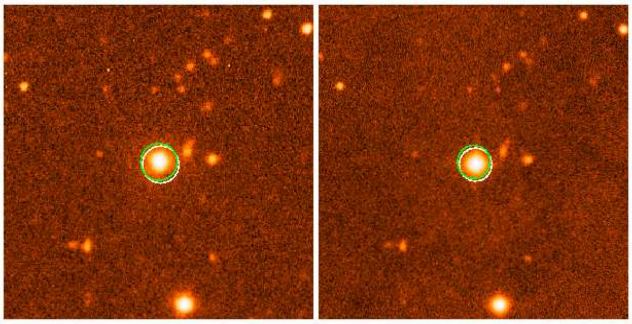

Figure 2.10: Candidate 3: this object is located in patch D and has an apparent I magnitude of 15.0. It has a proper motion $\mu = 0.24''/yr$. It is also known from the NLTT as: 788-50.

candidate	α (J2000)	δ (J2000)	m_I	μ [$"\mathrm{yr}^{-1}$]
1	05:44:11.534	-24:33:03.57	15.3	0.76
2	05:34:05.769	-24:22:55.83	14.5	0.21
3	09:51:21.139	-21:13:39.27	15.0	0.24

Table 2.1: Results

2.6 Conclusions

The NLTT catalog states both candidate 2 and 3 as being spectral class m. Candidate 1 is also unlikely to be a white dwarf because of its brightness. This survey therefore, while sensitive to proper motions $0.2 \leq \mu[''yr^{-1}] \leq 5.0$, and magnitudes $10.5 \leq m_I \leq 21.0$ in an area of 10.5 square degrees resulted in no detection of possible halo white dwarfs.

I would like to thank the members of the OmegaCAM group, in particular Danny Boxhoorn, Kor Begeman and Roeland Rengelink for the useful discussions I had with them and their help during this project.

Appendix A

SExtractor

This appendix gives a short explanation of SExtractor in general, the way it was used in this project and the relevant parameters calculated by the program. Many abilities and options of SExtractor are not mentioned here, only the configuration used in this project is described.

SExtractor is a source extraction program; it can detect objects in CCD (and other) images and calculate a large range of quantities, from their position to magnitudes, provided the input image has the necessary information stored in the FITS header. Specifically, SExtractor defines a collection of pixels as an object if:

1. the pixels have values greater than a given value times the standard deviation of the local background
2. the pixels are connected by their edges or corners
3. the number of such pixels is larger than a given number

A background map for the entire image is created, because in order to detect the faintest objects and determine their photometry accurately the background at any place in the image has to be known. This process is controlled by the following parameters:

- BACK_SIZE size of the background mesh in pixels, **50**
- BACK_FILTERSIZE size (in background meshes) of the background-filtering mask, **5**

The final background map is determined by a bicubic-spline interpolation between the meshes of the grid. The detection of objects is controlled most directly by:

- DETECT_THRESH detection threshold relative to background RMS, **1.5**
- DETECT_MINAREA min. number of pixels above the threshold to trigger a detection, **5**

A number of parameters are derived from the pixels constituting objects as defined above (i.e. S). The position of an object is described by the first order moments of the pixels (barycenter):

$$X = \bar{x} = \frac{\sum_{i \in S} I_i x_i}{\sum_{i \epsilon S} I_i} \tag{A.1}$$

$$Y = \bar{y} = \frac{\sum_{i \in S} I_i y_i}{\sum_{i \epsilon S} I_i} \tag{A.2}$$

An ellipse is associated with each object. This ellipse is a measure of the size and shape of an object. The semi-major axis A and semi-minor axis B as well as an angle THETA are derived from the second order moments of the pixels:

$$X2 = \overline{x^2} = \frac{\sum_{i \in S} I_i x_i^2}{\sum_{i \in S} I_i} - \bar{x}^2 \tag{A.3}$$

$$Y2 = \overline{y^2} = \frac{\sum_{i \in S} I_i y_i^2}{\sum_{i \in S} I_i} - \bar{y}^2 \tag{A.4}$$

$$XY = \overline{xy} = \frac{\sum_{i \in S} I_i x_i y_i}{\sum_{i \in S} I_i} - \bar{x}\bar{y} \tag{A.5}$$

And given as follows:

$$A^2 = \frac{\overline{x^2} + \overline{y^2}}{2} + \sqrt{(\frac{\overline{x^2} - \overline{y^2}}{2})^2 + \overline{xy}^2} \tag{A.6}$$

$$B^2 = \frac{\overline{x^2} + \overline{y^2}}{2} - \sqrt{(\frac{\overline{x^2} - \overline{y^2}}{2})^2 + \overline{xy}^2} \tag{A.7}$$

$$\tan 2\theta = 2\frac{\overline{xy}}{\overline{x^2} - \overline{y^2}} \tag{A.8}$$

θ (THETA) is the angle of A w.r.t. the NAXIS1 axis ('x') of the image, measured counter-clockwise.

A range of other output parameters are calculated, among them MAG_AUTO, which is a magnitude resulting from an adaptive aperture photometry procedure, inspired by Kron's "first moment" algorithm (Kron 1980). In short:

1. The second order moments of the object profile are used to define an equivalent bivariate Gaussian profile with mean standard deviation σ_{ISO}.

2. An elliptical aperture whose ellipticity ϵ and position angle θ are defined by these moments is scaled to 6 σ_{ISO}. ($\sim$2 isophotal radii)

3. Within this aperture the "first moment" is computed as follows:

$$r_1 = \frac{\sum rI(r)}{\sum I(r)}$$

Kron showed that for stars and galaxy profiles convolved with Gaussian seeing an almost constant fraction of the flux is expected to lie within a circular aperture of radius kr_1, independently of their mag. The remains valid for an ellipse with ϵkr_1 and $\frac{1}{\epsilon}kr_1$ as principle axes. A balance between systematic and random errors is achieved for $k \approx 2$. With $k=2.5$ the mean fraction of flux lost is about 6%. In this project this value of k was used.

Appendix B

LDAC tools

Operations on catalogs are performed by LDAC. These include various simple algebraic operations on columns and the addition or removal of columns from catalogs. LDAC can also be used to associate sources in different catalogs based on their positions and shape parameters (as calculated by SExtractor). These parameters are A, B and THETA describing an ellipse, the shape of which is determined by the second order moments of the pixels belonging to an object. (See Appendix A.)

Three different types of association are defined:

Type 1 Object A's center position is within the bounds of object B's ellipse circumference, and vice versa

Type 2 Object A's center position is within the bounds of the object B's ellipse circumference. Object B's center position lies outside object A's ellipse circumference.

Type 3 Object A's center position is outside the bounds of object B's ellipse circumference and vice versa, but their ellipses overlap.

There are several parameters that control the association process, the following parameters are relevant for this project:

- INTER_COLOR_TOL, Extension factor to scale the ellipse parameters with before determining associations, **1.0**
- MIN_ELLIPS_DELTA, Exclude associated objects if the difference between their ellipticity exceeds this value, **1.0 (no selection)**
- ALLOW_EQUAL_FIELD_POS, Allow intra catalog associations, **NO**
- RA, World coordinate system center position of objects, **ALPHA_SKY**
- DEC, World coordinate system center position of objects, **DELTA_SKY**
- A_WCS, SExtractor object shape parameter semi major axis, **A_WORLD**

- B_WCS, SExtractor object shape parameter semi minor axis, **B_WORLD**
- THETAWCS, SExtractor position angle, **THETA_WORLD**

LDAC associate takes two (or more) catalogs as input and appends several columns with information about the associations. Most importantly two (or more) columns are added in which the Sequence Number of the associated object in the other catalog(s) is indicated. Alternatively LDAC can place the associated object pairs in a new catalog where all parameters are vectors of length two, containing the information for the paired objects.

Bibliography

Alcock et al. (2000). The macho project: Microlensing results from 5.7 years of large magellanic cloud observations. *ApJ 542*, 281–307.

Benoist et al. (1999). Eso imaging survey vi. i-band data of patches c and d. *ApJ 346*, 58–66.

Bertin, E. (2002). Swarp v1.34 user's guide.

Bertin, E. and S. Arnouts (1996). Sextractor: software for source extraction. *A & A 117*, 393–394.

Bracewell, R. N. (1965). *The Fourier Tranform and its Applications* (Third Edition ed.). McGraw-Hill Higher Education.

Brault, J. W. and O. R. White (1971). The analysis and restoration of astronomical data via the fast fourier transform. *A & AS 13*, 169–189.

Deul, E. (1993). Denis - deep near infra-red survey of the southern sky. In *Astronomical Data Analysis and Processing Software II*, Volume 52. ASP Conference Series.

Ibata et al. (2000). Discovery of high proper-motion ancient white dwarfs: nearby massive compact halo objects? *ApJ 532*, L41–L45.

Kron, R. G. (1980). Photometry of a complete sample of faint galaxies. *ApJ SS 43*, 305–325.

Luyten, W. J. (1979). *New Luyten Catalgue of stars with proper motions larger than two tenths of an arcsecond*. Univ. of Minnesota Press, Minneapolis, MN.

Manfroid, J. (1995). Stellar calibration of ccd flat fielding. *A & AS 113*, 587–591.

Manfroid, J. (1996). On ccd standard stars and flat-field calibration. *A & AS 118*, 391–395.

N. Kaiser, G. Squires, T. B. (1995). A method for weak lensing observations. *ApJ 449*, 460–475.

Newberry, M. V. (1991). Signal-to-noise considerations for sky-subtracted ccd data. *PASP 103*, 122–130.

Oppenheimer et al. (2001). Direct detection of galactic halo dark matter. *Science 292*, 698–702.

R. A. Knox, M. R. S. Hawkins, N. C. H. (1999). A survey for cool white dwarfs and the age of the galactic disc. *MNRAS 306*, 736–752.

R. Di Stefano (2000). On the nature and location of the microlenses. *ApJ 541*, 587–596.

Stetson, P. B. (1993). Further progress in ccd photometry. In C. J. Butler and I. Elliot (Eds.), *Stellar photometry - Current techniques and future developments*, Volume 136, pp. 291. IAU Coll.: Cambridge University Press.

Tobin, W. (1993). Problems of ccd flat fielding. In C. J. Butler and I. Elliot (Eds.), *Stellar photometry - Current techniques and future developments*, Volume 136, pp. 304. IAU Coll.: Cambridge University Press.